



## Coking and sintering progress of a Ni supported catalyst in the steam reforming of biomass pyrolysis volatiles



Aitor Ochoa\*, Aitor Arregi, Maider Amutio, Ana G. Gayubo, Martín Olazar, Javier Bilbao, Pedro Castaño

Department of Chemical Engineering, University of the Basque Country (UPV/EHU), P.O. Box 644-48080, Bilbao, Spain

### ARTICLE INFO

**Keywords:**  
Biomass  
Steam reforming  
Deactivation  
Coke deposition  
Metallic sintering

### ABSTRACT

The valorization of biomass (pine wood) for hydrogen production has been studied in a two-step process, comprising pyrolysis and subsequent steam reforming of the volatiles produced in the first step. This work focuses on the deactivation of the Ni commercial catalyst used in the second step. Pyrolysis of biomass has been performed in a conical spouted bed reactor at 500 °C, and the in-line catalytic steam reforming of the pyrolysis volatiles, in a fluidized bed reactor at 600 °C. Deactivated catalyst samples were recovered at different values of time on stream, and analyzed by means of XRD, N<sub>2</sub> adsorption-desorption, SEM and TEM microscopies, TPO, Raman and FTIR spectroscopies. The results show that the deactivation is mainly due to the encapsulation of Ni particles by coke, together with Ni sintering, to a lesser extent (from a Ni particle size of 25 nm in the reduced fresh catalyst, to 39 nm at 100 min). The former is ascribed to the condensation of oxygenates (particularly phenols), and the latter is inevitable within the current conditions. As the fraction of uncovered Ni particles decreases with time on stream, the deposition of encapsulating coke is slowed down (from a formation rate of 0.30 mg<sub>coke</sub> g<sub>catalyst</sub><sup>-1</sup> min<sup>-1</sup> to 0.20 mg<sub>coke</sub> g<sub>catalyst</sub><sup>-1</sup> min<sup>-1</sup>, at 0–50 min and 50–100 min on stream, respectively), promoting the deposition of coke on the catalyst support (with a formation rate of 1.04 mg<sub>coke</sub> g<sub>catalyst</sub><sup>-1</sup> min<sup>-1</sup> at 50–100 min on stream), with a more carbonized structure and formed through the thermal decomposition of phenols in the reaction medium.

### 1. Introduction

The environmentally friendly nature of hydrogen has attracted significant interest as an energy carrier in the future [1]. Hydrogen combustion only generates water as product, thus resulting in a considerable reduction of the emissions of greenhouse gases into the atmosphere [2]. Moreover, the higher energy density of hydrogen (121 MJ kg<sup>-1</sup>) compared to other renewable fuels needs to be highlighted [3]. Nevertheless, hydrogen production is currently limited to the steam reforming of non-renewable sources, such as natural gas, naphtha and heavy oils [4]. In this scenario, the role of biomass as a renewable energy source is of especial relevance, given that its carbon-neutral nature leads to the reduction of CO<sub>2</sub> emission levels [2].

The thermochemical routes for biomass valorization (mainly pyrolysis and gasification) are characterized by their industrial scalability [5]. Berdugo Vilches et al. obtained a H<sub>2</sub> production of 2.2 wt% (based on biomass mass) in a 300 kg h<sup>-1</sup> gasification plant using olivine as catalyst [6]. A maximum H<sub>2</sub> production of 6.4 wt% was obtained by Umeki et al. operating in a demonstration plant with a feeding rate of

1.2 t/day [7]. Moreover, Madadian et al. concluded that H<sub>2</sub> production depends on the biomass feedstock, obtaining different H<sub>2</sub>/CO ratios when different biomass feedstocks were used in a 10 kWth pilot plant [8]. Although biomass gasification [9–12] and the indirect bio-oil reforming [13–16] are the most studied thermochemical routes in the literature, the novel strategy of biomass pyrolysis and the in-line catalytic steam reforming of the pyrolysis volatiles has proven to be suitable as an alternative route for hydrogen production [17–21]. The two-step pyrolysis-reforming studies are still performed in laboratory scale units, and most of the pyrolysis-reforming studies are carried out as two discontinuous systems; however, great progress has been made recently with the implementation of continuous biomass feeding into an in-line two-step strategy, obtaining H<sub>2</sub> productions around 10 wt%. This two-step process allows obtaining a free-tar gas with high H<sub>2</sub> content, operating at lower temperatures compared to gasification and avoiding intrinsic operational problems of the bio-oil and its vaporization.

In previous works, the combination of the conical spouted bed reactor and fluidized bed reactor showed good performance for the pyrolysis and in-line reforming step, respectively [22–24]. Furthermore,

\* Corresponding author.

E-mail address: [aitor.ochoa@ehu.eus](mailto:aitor.ochoa@ehu.eus) (A. Ochoa).

the versatility of this two-step process lies in the fact that different wastes and feeds can be valorized, such as biomass [25], different plastics [23,24,26] and biomass/plastic mixtures [27].

Nickel-based catalysts have been widely used in the literature for steam reforming of oxygenates, due to a high C–C bond-breaking activity and a relatively low cost [28,29]. However, although high conversion and hydrogen yields can be achieved, deactivation of Ni catalysts in reforming reactions have been widely reported to take place mainly by means of Ni sintering, and more significantly, by coke deposition [28,30–32], which is especially notorious when biomass is in the feed, due to the oxygenated nature of pyrolysis volatiles [33]. Some authors have identified two differentiated coke morphologies: (i) an amorphous or encapsulating coke, responsible for the obstruction of metallic sites, and (ii) a structured or filamentous coke, whose contribution to the catalyst performance is hardly noticeable [16,34–37], unless a massive growth of filaments takes place, hindering the access of reactants to the active sites [38]. Additionally, other authors have identified different fractions corresponding to coke with no particular morphology and deposited (i) on metal particles, (ii) on metal–support interface and (iii) on support [39–42]. Moreover, considering the fact that Ni catalyzes coke gasification and/or combustion, these authors conclude that coke deposited on metal particles have a lighter and disordered nature, whereas that deposited on support has a more carbonized and structured nature. Nevertheless, the complexity in the composition of volatilized biomass oxygenates (comprising acids, ketones, alcohols, esters and phenols, among others) calls for a step forward into the understanding of coke formation mechanisms [37,43]. In a previous study during the steam reforming of bio-oil, it was established that bio-oil oxygenates are the precursors of the Ni-encapsulating coke responsible for a high catalyst deactivation, among which phenols (including methoxyphenols) have the greatest impact [37]. Furthermore, sintering is recognized to become an important deactivation cause above 600–700 °C in Ni catalysts, depending on the catalyst structure, the operating conditions and the reaction medium composition [29,40,41,43].

This work focuses on the evolution of catalyst deactivation used in the second step of the sequenced pyrolysis-reforming of biomass (pine wood) for hydrogen production, in order to enhance its feasibility in a larger scale. For this aim, we have used the same system used by Arregi et al. [25,27,33], monitoring the evolution of catalyst structure and coke morphology at different stages of deactivation, i.e. different values of time on stream. The dynamics of catalytic deactivation have been studied by means of X-ray diffraction (XRD), N<sub>2</sub> adsorption-desorption, scanning and transmission electron microscopies (SEM and TEM, respectively), temperature programmed oxidation (TPO), Raman spectroscopy and Fourier transformed infrared (FTIR) spectroscopy. A simplified mechanism of catalyst deactivation is suggested, as well as several proposals for minimizing the impact of deactivation.

## 2. Experimental

### 2.1. Materials

The main properties of the pine wood (*pinus insignis*) used in this study are summarized in Table 1. The ultimate and proximate analyses have been determined in a LECO CHNS-932 elemental analyzer and TGA Q5000IR thermogravimetric analyzer, respectively, and the higher heating value (HHV) has been measured in a Parr 1356 isoperibolic bomb calorimeter. The biomass has been crushed and ground to a particle size between 1 and 2 mm and has been dried to a moisture content below 10 wt%.

The reforming of biomass pyrolysis volatiles has been carried out on a Ni commercial catalyst (ReforMax<sup>®</sup> 330 or G90LDP), whose chemical formulation is based on NiO, CaAl<sub>2</sub>O<sub>4</sub> and Al<sub>2</sub>O<sub>3</sub>. The original catalyst has a shape of perforated rings (19 × 16 mm) with a metallic phase of Ni supported on Al<sub>2</sub>O<sub>3</sub>, which is doped with Ca, with the NiO content

**Table 1**  
Biomass characterization.

Ultimate analysis (wt%)	
Carbon	49.33
Hydrogen	6.06
Nitrogen	0.04
Oxygen	44.57
Proximate analysis (wt%)	
Volatile matter	73.4
Fixed carbon	16.7
Ash	0.5
Moisture	9.4
HHV (MJ kg <sup>-1</sup> )	19.8

Note: the values in the ultimate analysis are ash-free.

being 14%. This catalyst was ground and sieved to 0.4–0.8 mm, which is the suitable particle size to attain stable fluidization regime.

### 2.2. Operating conditions, composition of the stream into the reforming step and reaction indices

The pyrolysis and in-line catalytic steam reforming process has been performed in a bench scale plant, whose general scheme and components have been described elsewhere [25].

The operating conditions used in the pyrolysis of biomass (conical spouted bed) are as follows: 500 °C, biomass feed rate, 0.75 g min<sup>-1</sup>; water flow rate, 3 ml min<sup>-1</sup>; sand bed, 50 g; sand particle size, 0.3–0.35 mm. Table 2 shows the product distribution obtained in the pyrolysis of biomass in the conical spouted bed reactor, this stream being continuously fed into the reforming step. The volatile stream from biomass pyrolysis is mainly composed of oxygenated volatiles, which have been classified in the following functional groups [44]: phenols (whose content is the highest among all, 16.5 wt%), ketones, saccharides, furans, acids, alcohols and aldehydes. Moreover, the stream has a high water content (25.4 wt%), CO and CO<sub>2</sub> (products from the partial decarbonylation and decarboxylation of the oxygenates), as well as low concentrations of C<sub>1</sub>–C<sub>4</sub> hydrocarbons (products from cracking processes).

The reforming conditions of biomass pyrolysis volatiles are: 600 °C, space time, 20 g<sub>catalyst</sub> min g<sub>volatiles</sub><sup>-1</sup>; steam/biomass mass ratio fed into the pyrolysis step, 4 (steam/carbon molar ratio fed into the reforming step, 7.7). Catalyst deactivation implies a decrease in the rates of the main reactions involved in the reforming process, namely reforming of bio-oil oxygenates (Eq. (1)) and water gas shift (WGS) reaction (Eq. (2)).

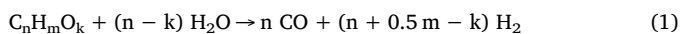


**Table 2**  
Yields of biomass pyrolysis products (wt%).

Compound	Yield (wt%)
Gas	7.3
CO	3.38
CO <sub>2</sub>	3.27
Hydrocarbons (C <sub>1</sub> –C <sub>4</sub> )	0.68
Volatiles	75.3
Acids	2.73
Aldehydes	1.93
Alcohols	2.00
Ketones	6.37
Phenols	16.49
Furans	3.32
Saccharides	4.46
Water	25.36
Char	17.3



In order to quantify the deactivation, the following reaction indices have been defined: conversion and yields of C containing species and H<sub>2</sub>.

The conversion (Eq. (3)) is defined as the ratio between the carbon units recovered in the gaseous fraction and entering the reforming step.

$$X (\%) = \frac{\text{carbon units in the product gas stream}}{\text{carbon units in the volatiles feed stream}} \cdot 100 \quad (3)$$

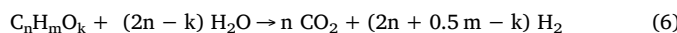
The yield of each compound containing carbon (Eq. (4)) is defined as the ratio between the molar flow rates of product *i* and those fed into the reforming step, both given in carbon units contained.

$$Y_i (\%) = \frac{\text{carbon units in the product}}{\text{carbon units in the volatiles feed stream}} \cdot 100 \quad (4)$$

The H<sub>2</sub> yield (Eq. (5)) is determined as a percentage of the maximum allowable by stoichiometry,

$$Y_{H_2} (\%) = \frac{F_{H_2}}{F_{H_2}^0} \cdot 100 \quad (5)$$

where  $F_{H_2}$  is the molar flow of hydrogen in the product stream and  $F_{H_2}^0$  is that corresponding to the stoichiometric maximum, referred to the volatiles feed stream in the steam reforming step. The stoichiometry is shown in Eq. (6), obtained from Eqs. (1) and (2):



### 2.3. Characterization of fresh and used catalyst

The deactivation study was performed with runs at different time on stream values up to 100 min, with the aim of analyzing the catalyst in different deactivation degrees. The fluidized bed system in this work has led to a uniform catalyst activity, attaining standard deviations below 5% between the runs. After each run, the deactivated catalyst was withdrawn from the system and subsequently analyzed, its representativeness being guaranteed due to the fluidized bed system and the uniform catalyst activity.

Catalyst characterization was performed by means of several techniques: (i) the evolution of catalyst crystallographic structure and Ni<sup>0</sup> particle size was analyzed by XRD; (ii) the evolution of surface properties and both catalyst and coke morphology was studied by N<sub>2</sub> adsorption-desorption and SEM and TEM electro microscopy; (iii) the evolution of coke content, structuring and composition was studied by temperature programmed oxidation (TPO), Raman and FTIR spectroscopy.

XRD analysis was performed in a Philips X'PERT PRO diffractometer, operating at 40 kV and 40 mA, in theta-theta configuration, with a secondary monochromator with CuK $\alpha_1$  radiation, at a wavenumber of 1.5418 Å. An energy dispersive PIXcel detector was used with an active length of  $2\theta = 3.347$  Å. The average Ni<sup>0</sup> particle size was determined by applying the Debye-Scherrer approach at  $2\theta = 52^\circ$ , corresponding to Ni<sup>0</sup> (200) plane.

The surface area, pore volume, and average pore size of the catalyst were measured by N<sub>2</sub> adsorption-desorption in a Micromeritics ASAP 2010 system by means of the conventional Brunauer-Emmett-Teller (BET) method. Experimental procedure consists on a degasification step at 150 °C during 8 h, followed by N<sub>2</sub> (99.9995%) adsorption-desorption.

SEM images were obtained in a JEOL JSM-7000F microscope with a tungsten filament (resolution 3.5 nm) equipped with an Oxford Pentafet energy-dispersive X-ray spectroscopic (EDX) analyzer (resolution 133 eV), operating at 20 kV, under vacuum at  $9.65 \cdot 10^{-5}$  bar and intensity of  $1.85 \cdot 10^{-10}$  A.

TEM images were obtained in a Philips SuperTwin CM200 microscope equipped with a LaB<sub>6</sub> filament and EDAX EDX microanalysis system, operating at 200 kV. Samples for the analysis were prepared via

dispersion in ethanol solvent and deposition of a suspension drop on a carbon-coated copper grid (300 Mesh) followed by drying under vacuum.

TPO analysis was carried out in a Thermo Scientific TGA Q5000TA IR system, coupled on line with a Balzer Instruments Thermostar mass spectrometer in order to follow the evolution of combustion gases (mainly CO<sub>2</sub>). Ground sample (5 mg) was first degasified with an inert 10 ml min<sup>-1</sup> stream (N<sub>2</sub>) for 5 min, and subsequently a 50 ml min<sup>-1</sup> air stream was introduced, from 100 °C to 700 °C with a heating rate of 5 °C min<sup>-1</sup>. The coke content was quantified from the CO<sub>2</sub> signal in the mass spectrometer during combustion, instead of the thermogravimetric signal, because Ni oxidation masks the latter signal.

Raman spectroscopic analysis were performed in a Renishaw InVia confocal microscope using an excitation wavelength of 514 nm, performing the analysis in several areas of the sample for increased reproducibility.

FTIR spectroscopy was carried out in a FTIR Nicolet 6700 spectrometer, in transmission mode. Prior to the analysis of the deactivated sample, in order to subtract the influence of the catalyst on the FTIR spectrum, a sample is pelletized and analyzed, consisting of fresh catalyst (3–5 mg) on a KBr support (150 mg, purity above 99%), prepared by applying a pressure of 10 t cm<sup>-2</sup> for 15 min. Subsequently, a pellet sample consisting of 3–5 mg of deactivated catalyst on a 150 mg of KBr support was prepared and analyzed after subtraction of the former sample signal.

## 3. Results

### 3.1. Evolution with time on stream of reaction indices

Fig. 1 shows the effect of catalyst deactivation in the evolution of reaction indices with time on stream. H<sub>2</sub> and CO<sub>2</sub> yields follow a similar decreasing trend to that of conversion, due to the fact that deactivation disfavors steam reforming reaction (Eq. (1)), as well as WGS reaction (Eq. (2)). Consequently, yields of CH<sub>4</sub> and C<sub>2</sub>-C<sub>4</sub> hydrocarbons increase over time. Interestingly, the decrease in the reaction indices is approximately linear up to 50 min of time on stream and subsequently decreases more rapidly, since the conversion of biomass pyrolysis volatiles and yields of H<sub>2</sub> and CO<sub>2</sub> decrease more rapidly, whereas the

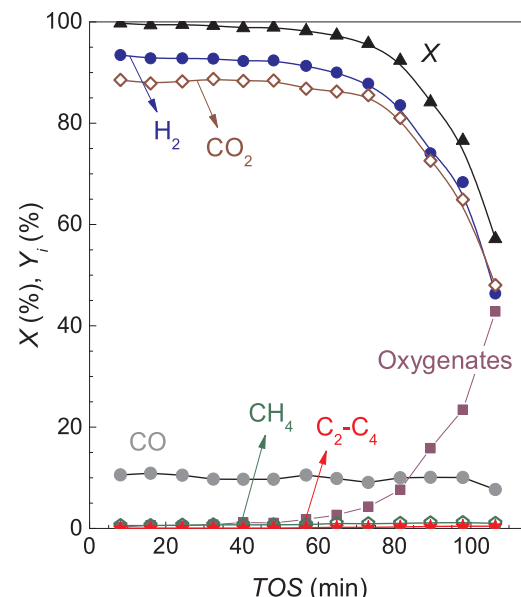
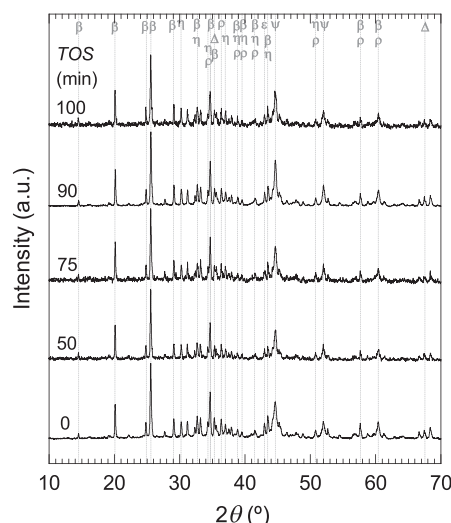


Fig. 1. Evolution with time on stream of the conversion of volatiles from biomass pyrolysis (X) and yield of products (Y<sub>i</sub>). Operating conditions: temperature, 600 °C; space time, 20 g<sub>catalyst</sub> min g<sub>volatiles</sub><sup>-1</sup>; steam/carbon molar ratio, 7.7.



**Fig. 2.** XRD spectra of the reduced fresh catalyst (0 min) and deactivated at several values of time on stream. Assigned bands:  $\text{Ni}^\circ$  ( $\psi$ );  $\text{NiO}$  ( $\varepsilon$ );  $\text{Al}_2\text{O}_3$  ( $\Delta$ );  $\text{CaO}(\text{Al}_2\text{O}_3)_2$  ( $\beta$ ),  $\text{CaAl}_2\text{O}_4$  ( $\eta$ );  $\text{CaAl}_{12}\text{O}_{19}$  ( $\rho$ ).

yields of  $\text{CH}_4$  and  $\text{C}_2\text{-C}_4$  increase slightly quicker with time on stream. The catalyst deactivation leads to an exponential increase of the non-reacted oxygenates, which are the precursors of coke formation, and this in turn promotes a higher deactivation, giving as a result the observed autocatalytic effect in the deactivation trend. Additionally, the yield of  $\text{CO}$  follows an approximately steady trend with time of stream, due to the contrary effects of the deactivation of steam reforming and water gas shift. Thus, the deactivation has two stages, with the change at ca. 50 min on stream.

### 3.2. Evolution of $\text{Ni}$ particles

Fig. 2 shows the XRD diffractograms corresponding to reduced fresh catalyst and deactivated at several values of time on stream. The diffractograms show the assignment of several peaks at different diffraction angles ( $2\theta$ ) to a total of six crystalline phases, expressed as Greek symbols at the top of Fig. 2. The assignment was carried out as follows [29,37,43]:  $\text{Ni}^\circ$ ,  $44.7^\circ$  in (111) plane and  $52^\circ$  in (200) plane (JCPDS 00-004-0850);  $\text{NiO}$ ,  $43^\circ$  (JCPDS 00-047-1049);  $\text{Al}_2\text{O}_3$ ,  $35.4^\circ$  and  $67.3^\circ$  (JCPDS 01-086-1410);  $\text{CaO}(\text{Al}_2\text{O}_3)_2$ ,  $14.4^\circ$ ,  $20^\circ$ ,  $24.6^\circ$ ,  $25.6^\circ$ ,  $32.8^\circ$ ,  $34.5^\circ$ ,  $35.4^\circ$ ,  $37.7^\circ$ ,  $39.4^\circ$ ,  $41.4^\circ$ ,  $43.3^\circ$ ,  $57.4^\circ$  and  $60.3^\circ$  (JCPDS 01-071-2090);  $\text{CaAl}_2\text{O}_4$ ,  $30.1^\circ$ ,  $32.8^\circ$ ,  $34.2^\circ$ ,  $36.9^\circ$ ,  $37.7^\circ$ ,  $39.4^\circ$ ,  $41.4^\circ$ ,  $43.3^\circ$  and  $50.6^\circ$  (JCPDS 00-023-1036);  $\text{CaAl}_{12}\text{O}_{19}$ ,  $34.2^\circ$ ,  $36.2^\circ$ ,  $37.7^\circ$ ,  $39.4^\circ$ ,  $41.4^\circ$ ,  $50.6^\circ$ ,  $57.4^\circ$  and  $60.3^\circ$  (JCPDS 01-084-1613). This assignment leads to an overlapping of several phases in the same  $2\theta$  positions. XRD spectra indicate the presence of  $\text{Ni}^\circ$  crystalline phases which conserve their reduced state during the reaction, indicated by the low intensity of the  $\text{NiO}$  peak at  $2\theta = 43^\circ$ . This is due to the reducing capacity of  $\text{H}_2$  and  $\text{CO}_2$  in the employed reaction conditions, as well as the capacity of the formed coke to maintain  $\text{Ni}$  in its reduced state, even when the catalyst is extracted to the oxidant atmosphere [45].

$\text{Ni}^\circ$  crystal size was calculated considering the Debye-Scherrer approach at  $2\theta = 52^\circ$ , corresponding to  $\text{Ni}^\circ$  (200) plane, whose evolution is shown in Fig. 3. An increasing trend is observed in the size with time on stream, from 25 nm in the reduced fresh catalyst, to 39 nm at 100 min. These results evidence that  $\text{Ni}$  is sintering at  $600^\circ\text{C}$  [28], with an approximately linear sintering rate of ca.  $5 \text{ nm h}^{-1}$  in the first 100 min, although a trend toward a steady  $\text{Ni}$  particle size is expected at higher values of time on stream. This behavior was also observed employing the same catalyst in the steam reforming of volatiles from polyethylene pyrolysis at  $700^\circ\text{C}$  [43], with faster sintering rate (ca.  $20 \text{ nm h}^{-1}$ ), due to the higher temperature used, which has a critical

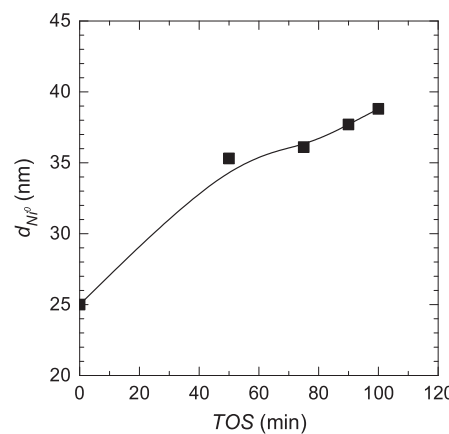


**Fig. 3.** Evolution with time on stream of  $\text{Ni}^\circ$  crystal size of the fresh reduced and deactivated catalysts, determined by XRD.

**Table 3**

Evolution with time on stream of the surface physical properties of the catalyst.

TOS (min)	$S_{\text{BET}}$ ( $\text{m}^2 \text{g}^{-1}$ )	$V_{\text{pore}}$ ( $\text{cm}^3 \text{g}^{-1}$ )	$d_{\text{pore}}$ ( $\text{\AA}$ )
0	19.0	0.111	122
50	10.2	0.072	292
75	13.8	0.081	257
90	18.0	0.114	285
100	17.1	0.101	243

role in sintering [32,46].

### 3.3. Evolution of catalyst morphology

Table 3 depicts the evolution with time on stream of the surface and structural properties of the catalyst, namely, surface area ( $S_{\text{BET}}$ ), pore volume ( $V_{\text{pore}}$ ) and average pore size ( $d_{\text{pore}}$ ), determined from  $\text{N}_2$  adsorption-desorption isothermal curves. The results show a sharp change of the catalyst porous structure at 50 min of time on stream, with a decrease in surface area from  $19 \text{ m}^2 \text{g}^{-1}$  in the reduced fresh catalyst, to  $10.2 \text{ m}^2 \text{g}^{-1}$ . At the same time, total pore volume is decreased from  $0.111 \text{ cm}^3 \text{g}^{-1}$  to  $0.072 \text{ cm}^3 \text{g}^{-1}$  and the average pore size is increased from  $122 \text{\AA}$  to  $292 \text{\AA}$  in the deactivated catalyst. These results suggest a blockage by coke deposition of the catalyst mesopores and micropores, being the latter preferentially blocked. Between 50 min and 90 min, an overall increasing trend of the surface area is observed, from  $10.2 \text{ m}^2 \text{g}^{-1}$  at 50 min, to  $18.0 \text{ m}^2 \text{g}^{-1}$  at 90 min, the total pore volume is increased from  $0.072 \text{ cm}^3 \text{g}^{-1}$  to  $0.114 \text{ cm}^3 \text{g}^{-1}$  and the average pore size is decreased from  $292 \text{\AA}$  to  $285 \text{\AA}$ . These results suggest that between 50 min and 90 min, the continuous deposition of coke creates a more porous structure on the catalyst surface. Interestingly, at 90 min the porous coke surface attains both similar surface area and total pore volume to those of the reduced fresh catalyst (from  $19.0 \text{ m}^2 \text{g}^{-1}$  to  $18.0 \text{ m}^2 \text{g}^{-1}$ , and from  $0.111 \text{ cm}^3 \text{g}^{-1}$  to  $0.114 \text{ cm}^3 \text{g}^{-1}$ , respectively). From 90 min to 100 min, the surface area, the total pore volume and the average pore diameter are slightly decreased, from  $18.0 \text{ m}^2 \text{g}^{-1}$  to  $17.1 \text{ m}^2 \text{g}^{-1}$ , from  $0.114 \text{ cm}^3 \text{g}^{-1}$  to  $0.101 \text{ cm}^3 \text{g}^{-1}$ , and from  $285 \text{\AA}$  to  $243 \text{\AA}$ , respectively), presumably due to a change in the structure of the coke deposited.

Fig. 4 shows SEM images of the fresh catalyst (Fig. 4a) and deactivated at several values of time on stream (Fig. 4b–e): 50, 75, 90 and 100 min. The fresh catalyst in Fig. 4 shows dispersed  $\text{Ni}$  particles on its surface, which have been identified by backscattered electron microscopy (not shown), and the catalyst surface shows certain roughness. At 50 min, this surface roughness is decreased, as flatter surfaces are observed in Fig. 4b, suggesting a surface blockage by the coke deposited, in line with the results by  $\text{N}_2$  adsorption-desorption in Table 3. Above

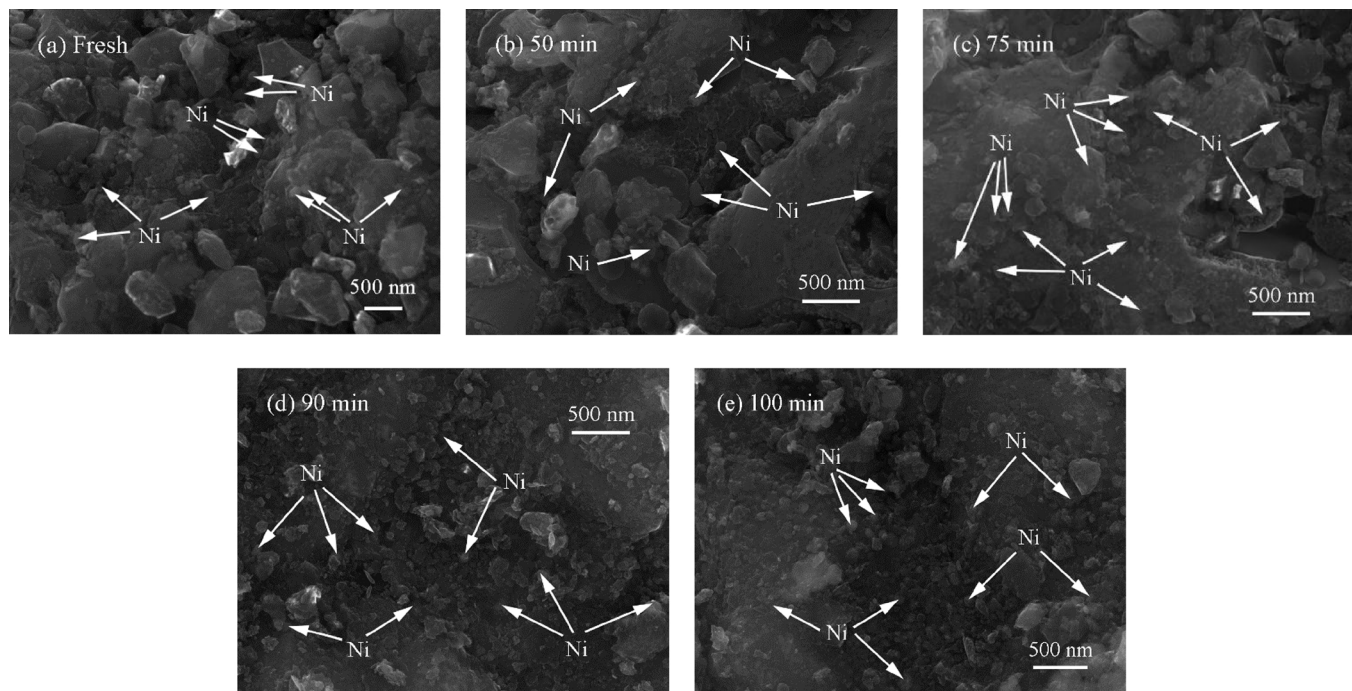


**Fig. 4.** SEM images of the fresh catalyst (a) and deactivated at several values of time on stream: 50 min (b); 75 min (c); 90 min (d); 100 min (e).

50 min, coke continues depositing and creates rougher surfaces, as observed at 90 and 100 min (Fig. 4d–e), in contrast with 50 min and 75 min (Fig. 4b–c). This may be explained as a higher surface porosity (Table 3). Images corresponding to the deactivated catalysts (Fig. 4b–e) do not show any particular morphology in which coke is deposited on the catalyst surface. Additionally, the backscattered electron microscopic analysis (not shown) shows an increase in the blurring of Ni particles with time on stream, suggesting that coke is progressively deposited on the Ni particles.

Fig. 5 shows TEM images corresponding to the reduced fresh catalyst (Fig. 5a) and deactivated at representative values of time on stream, namely at 50, 75, 90 and 100 min (Fig. 5b–e).  $\text{Ni}^0$  particles are identified in the images in Fig. 5 as the round-shaped, darkest regions with a high definition. Fig. 6 shows the distribution of the particle size measured from a representative number of TEM images, corresponding to the reduced fresh and deactivated catalysts. The distribution of  $\text{Ni}^0$  particle sizes becomes higher and broader upon the increase of time on stream, i.e.  $\text{Ni}^0$  sintering leads to bigger and more diverse particles sizes. The 'x' symbols in Fig. 5e point two  $\text{Ni}^0$  particles close to each other, suggesting their mobility during the sintering process.

The main statistical parameters of the distribution curves shown in Fig. 6 are displayed in Table 4. The average  $\text{Ni}^0$  crystallite size values by TEM (Table 4) corroborate the observation by XRD (Fig. 3) of  $\text{Ni}^0$  sintering, with an approximate rate of  $8 \text{ nm h}^{-1}$  in the studied region of time on stream. Nevertheless, the average values by TEM are slightly higher than those determined by XRD. This is recognized in the literature to be due to defects in the crystalline structure not quantified by XRD [47,48], thus resulting in a lower  $\text{Ni}^0$  particle size calculated by XRD. Moreover, the increasing standard deviation in Table 4 quantifies the size broadening with time on stream observed in Fig. 6. A similar increasing evolution with time on stream of both average and standard deviation values of the  $\text{Ni}^0$  particle size was previously observed for the steam reforming of volatiles from polyethylene pyrolysis using a Ni commercial catalyst [43].

The TEM images in Fig. 5 of the catalyst deactivated at different values of time on stream also reveal the encapsulating nature of the coke deposited, in line with SEM images (Fig. 4b–e). At lower values of time on stream (50 min), coke is observed as an amorphous layer

covering the Ni particles (Fig. 5b), as well as covering the catalyst surface in the vicinities of the Ni particles. As time on stream is increased (after 50 min), the surface Ni particles are gradually covered, hampering the access of reactants to these active sites, and leading to a more significant catalyst deactivation, as observed in Fig. 1. Meanwhile, as the fraction of uncovered Ni particles is decreased, the deposition of coke further from Ni particles is increasingly favored with time on stream (Fig. 5c–e). Additionally, the zones with a lower contrast and definition in TEM images in Fig. 5 were identified as Ca and Al oxides in the catalyst, though the assignment of each oxide from the images is difficult.

#### 3.4. Evolution of coke deposition

Fig. 7 shows the TPO profiles of the used catalysts at different values of time on stream. The temperature of coke combustion is closely related with its composition and/or its location on the catalyst. Thus, in this type of metallic catalysts, a lower combustion temperature is associated with [34–36,49,50]: (i) more hydrogenated composition of coke (higher proportion of aliphatics with respect to aromatics, i.e., higher H/C relationship); (ii) more oxygenated composition (higher O/C relationship); and/or (iii) proximity of coke to metallic sites, which catalyze coke gasification in the steam reforming and/or coke combustion.

Some authors have attributed the observed deposition heterogeneity to differences in location, distinguishing between [39–42,51,52]: (i) coke deposited on metal particles, which is easily accessible to gasification during the steam reforming and to oxygen during its combustion, activated by these Ni particles; (ii) coke deposited on metal-promoter and/or metal-support interface; (iii) coke deposited on support, whose combustion is not catalytically activated, and oxygen accessibility may be hampered by the porous structure of the support. Conversely, other studies have ascribed the heterogeneity in the deposited coke to the presence of two differentiated morphologies, namely non-filamentous and filamentous coke, depending on a series of factors, such as the operating conditions, the composition of the feed or the catalyst structure, among others [37]. Moreover, it is generally accepted in the literature that the formation of filamentous coke takes place from: (i)

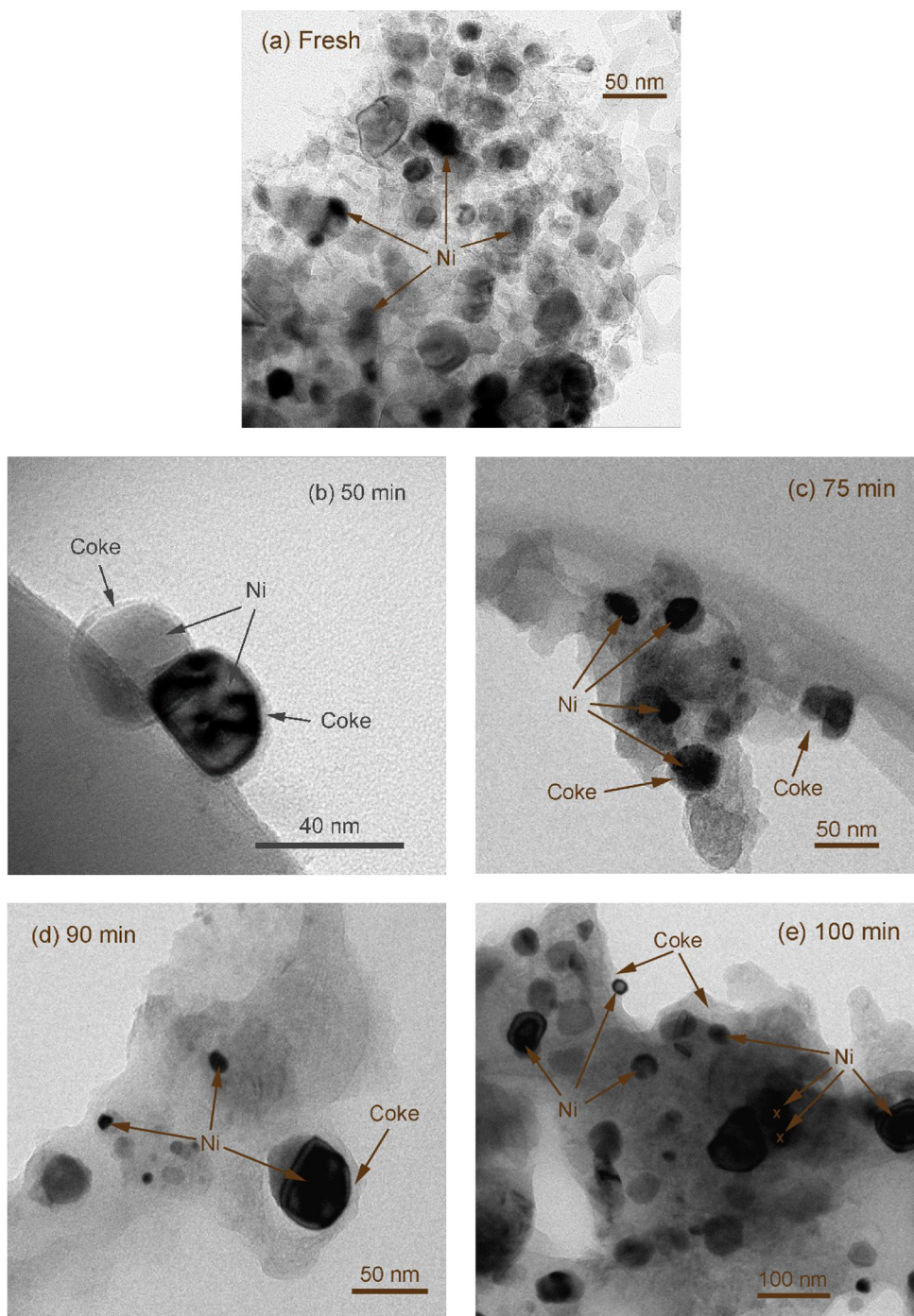


**Fig. 5.** TEM images of the fresh catalyst (a) and used at time on stream values of 50 min (b), 75 min (c), 90 min (d) and 100 min (e).

CO by the Boudouard reaction, (ii)  $\text{CH}_4$  by its decomposition and/or (iii) light hydrocarbons by their decomposition [37,43,53], and this coke may result in the separation of Ni crystallites from the support [36,54–56]. Nevertheless, giving that the yields of CO,  $\text{CH}_4$  and light hydrocarbons ( $\text{C}_2\text{-C}_4$ ) are considerably low and approximately steady in Fig. 1 (7.7%, 1% and 0.4%, respectively, at 100 min), this presumably explains the absence of any filamentous morphology. Therefore, only non-filamentous morphology is observed in the TEM images in Fig. 5, and thus, the two regions observed in the TPO profiles in Fig. 7 are thought to be mainly due to differences in coke composition (H/C and/or O/C relationship) and location on the catalyst surface.

Attending to the aforementioned circumstances in coke combustion, the first peak at ca. 420–430 °C is named coke I, whereas the second

peak at ca. 520–565 °C is named coke II. Generally, the combustion temperature of coke I (< 475 °C in Fig. 7), indicates one or a combination of the following features: (i) location on the metallic sites, which promote both coke combustion; and/or (ii) composition, with higher content of aliphatics, thus making it lighter, more amorphous and easier to burn off [34–37,43]. Coke I corresponds to the Ni encapsulating one, as observed in the TEM images (Fig. 5b–e), which directly hinders the reaction. On the other hand, the combustion temperature of coke II (> 475 °C in Fig. 7) indicates the presence of highly ordered aromatics and/or located at further distance from the Ni. This coke corresponds to that observed in the TEM images (Fig. 5b–e), whose combustion and/or gasification is not catalyzed.

Fig. 8 shows the evolution with time on stream of the content of

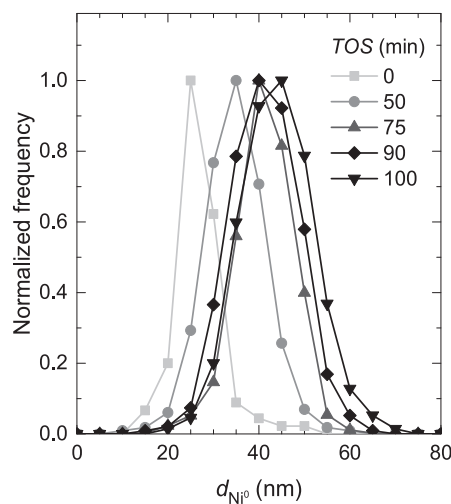


Fig. 6. Evolution with time on stream of the distribution of  $\text{Ni}^0$  crystal size of the catalyst, based on TEM images.

Table 4

Evolution with time on stream of the distribution of  $\text{Ni}^0$  crystallite size ( $d_{\text{Ni}^0}$ , nm), determined from TEM images.

TOS (min)	Average (nm)	Standard deviation (nm)
0	24	5.0
50	37	7.1
75	39	8.3
90	41	9.8
100	43	11

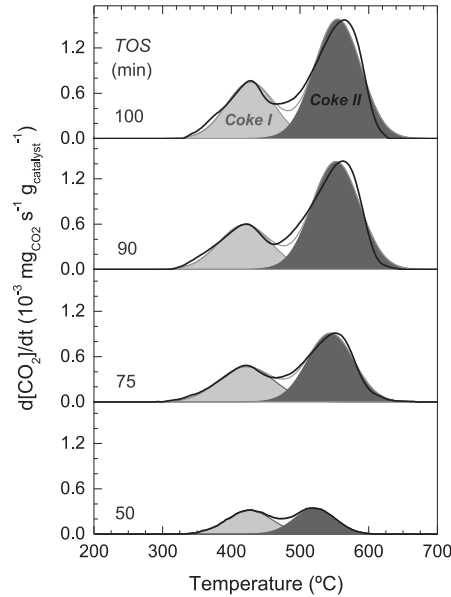


Fig. 7. Evolution with time on stream of the TPO profiles of coke combustion.

each coke type, obtained from the Gaussian fitting of the TPO profiles in Fig. 7. The total coke content follows a similar trend to that of the yield of non-reacted oxygenates in the reforming step (Fig. 1), since they are the precursors of coke formation. The evolution of coke I and II contents follow two different rates: 0–50 min, with coke formation rates of 0.30 and  $0.48 \text{ mg}_{\text{coker}} \text{ g}_{\text{catalyst}}^{-1} \text{ min}^{-1}$ , respectively; and 50–100 min, with the corresponding rates of 0.20 and  $1.04 \text{ mg}_{\text{coker}} \text{ g}_{\text{catalyst}}^{-1} \text{ min}^{-1}$ , respectively. These values reveal a decrease in the rate of formation of coke I from 50 min, whereas that for coke II is considerably increased

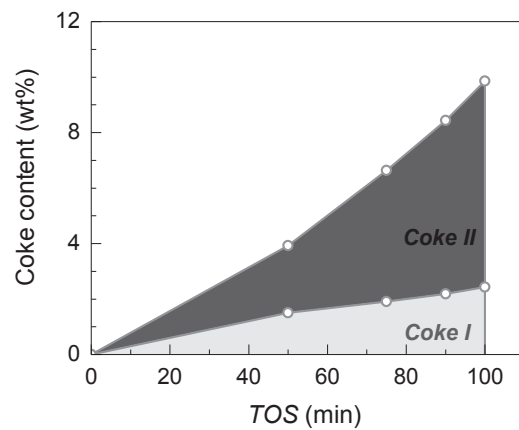


Fig. 8. Evolution with time on stream of the content of coke deposited on the catalyst.

from 50 min, leading to a coke content at 100 min approximately 3 times higher for coke II than that for coke I. These results can be explained as coke I is mainly deposited on the metallic sites, and thus its formation rate decreases with time on stream, as the fraction of uncovered metallic sites is decreased. Thus, as time on stream is increased, coke deposition mainly takes place in the vicinities of the metallic sites (coke II), on the promoter and/or support surface.

Interestingly, this change in the trend of the formation rate of both coke types at 50 min is in line with the change in the activity trend observed in Fig. 1, as the deactivation rate is considerably increased approximately above 50 min. As aforementioned and according to the literature [34–37, 57, 58], coke I corresponds to that covering the Ni particles, leading to the hindrance of the adsorption of reactants and a deep impact on catalyst deactivation. During the first 50 min on stream, the coke deposited on the metallic sites (coke I) is increased in content, but uncovered and active metallic sites are still available for reaction. After 50 min, the fraction of uncovered metallic sites is significantly reduced with time on stream, leading to an increase of the concentration of coke precursors in the reaction medium, and thus causing the deactivation behavior observed in Fig. 1.

In order to study the evolution with time on stream of the nature of both coke types, a kinetic study of the coke combustion has been performed, assuming the combustion profiles in Fig. 7 as the sum of two independent combustion steps. In a previous work [59], several methods for the calculation of kinetic data of combustion were described and compared, and a first order kinetic model is acceptable to describe the process. Thus, the overall rate of combustion conversion ( $-r_{i,\text{calc}}$ ) is as follows,

$$\begin{aligned}
 -r_{i,\text{calc}} &= \sum_{j=1}^2 (-r_i)_{j,\text{calc}} = \sum_{j=1}^2 \left( \frac{-dC_i}{dt} \right)_{j,\text{calc}} \\
 &= \sum_{j=1}^2 k_j^{T^\dagger} \cdot \exp \left[ \frac{-E_j}{R} \left( \frac{1}{T_i} - \frac{1}{T^\dagger} \right) \right] \cdot f_j \cdot C_i
 \end{aligned} \quad (7)$$

where  $k_j^{T^\dagger}$  is the kinetic constant,

$$k_j^{T^\dagger} = \kappa_j^{T^\dagger} \cdot P_O \quad (8)$$

and where  $i = 1, \dots, n$  is the point of data acquisition,  $n$  is the total number data adquisition points in the experiment,  $j$  is the number of coke fraction (1 or 2),  $\text{calc}$  stands for calculated combustion rate values,  $C$  is the coke content with respect to the catalyst mass (in  $\mu\text{g}_{\text{coker}} \text{ g}_{\text{catalyst}}^{-1}$ ),  $T^\dagger$  is the reference temperature (823 K in this work),  $k^{T^\dagger}$  is the apparent kinetic constant at the reference temperature (in  $\text{s}^{-1}$ ),  $\kappa^{T^\dagger}$  is the real kinetic constant at the reference temperature (in  $\text{atm}^{-1} \text{ s}^{-1}$ ),  $E$  is the activation energy (in  $\text{kJ mol}^{-1}$ ),  $f_j$  is the mass fraction each coke type with respect to the total coke content, and  $P_O$  is

**Table 5**

Evolution with time on stream of the kinetic parameters of coke combustion ( $k_1^{823K}$  and  $E$ ) for both coke types, fraction of coke I ( $f_1$ ) and objective function (OF) from Eq. (9), employing a first order model (Eq. (7)).

TOS (min)	$k_1^{823K}$ ( $\text{s}^{-1}$ )	$E_1$ ( $\text{kJ mol}^{-1}$ )	$k_2^{823K}$ ( $\text{s}^{-1}$ )	$E_2$ ( $\text{kJ mol}^{-1}$ )	$f_1$	OF ( $\mu\text{g}_{\text{coke}}^2 \text{s}^{-2} \text{g}_{\text{catalyst}}^{-2}$ )
50	$6.57 \cdot 10^{-2} \pm 3.07 \cdot 10^{-3}$	$116 \pm 1.1$	$2.34 \cdot 10^{-3} \pm 9.95 \cdot 10^{-6}$	$131 \pm 0.9$	$0.38 \pm 2.1 \cdot 10^{-3}$	$5.4 \cdot 10^{-5}$
75	$6.77 \cdot 10^{-2} \pm 3.38 \cdot 10^{-3}$	$119 \pm 1.2$	$2.18 \cdot 10^{-3} \pm 9.72 \cdot 10^{-6}$	$138 \pm 1.0$	$0.29 \pm 2.6 \cdot 10^{-3}$	$4.6 \cdot 10^{-5}$
90	$6.93 \cdot 10^{-2} \pm 4.59 \cdot 10^{-3}$	$120 \pm 1.6$	$1.86 \cdot 10^{-3} \pm 8.23 \cdot 10^{-6}$	$153 \pm 1.1$	$0.26 \pm 1.9 \cdot 10^{-3}$	$1.09 \cdot 10^{-4}$
100	$7.36 \cdot 10^{-2} \pm 5.23 \cdot 10^{-3}$	$131 \pm 1.9$	$1.77 \cdot 10^{-3} \pm 8.47 \cdot 10^{-6}$	$157 \pm 1.3$	$0.25 \pm 2.3 \cdot 10^{-3}$	$1.57 \cdot 10^{-4}$

the partial pressure of oxygen in the thermobalance (considered constant).

The kinetic parameters have been calculated by minimizing an objective function (OF) defined as the sum of the squares of the differences between experimental (exp) and calculated (calc) values of the combustion rate, obtained from Fig. 7 and Eq. (7), respectively, and expressed as follows:

$$OF = \sum_{i=1}^n \left[ \left( \frac{-dC_i}{dt} \right)_{\text{exp}} - \left( \frac{-dC_i}{dt} \right)_{\text{calc}} \right]^2 \quad (9)$$

The kinetic results from the fitting in Eq. (9) are shown in Table 5. The kinetic constant for coke I ( $k_1^{823K}$ ) is increased with time on stream, which as a general statement is thought to be related to lower combustion temperatures. At the same time, the activation energy for coke I ( $E_1$ ) shows an increasing trend, related to higher combustion temperatures. Thus, the combined effect of the evolution with time on stream of both  $k_1^{823K}$  and  $E_1$  leads to a synergy, resulting on an approximately steady value of the peak maximum position for coke I in Fig. 7. These results suggest that coke I changes in nature with time on stream, but do not imply significant changes in the combustion temperature. The kinetic parameters in Table 5 corresponding to the combustion of coke II show a decrease of the kinetic constant ( $k_2^{823K}$ ) and an increase of the activation energy ( $E_2$ ) with time on stream, both trends leading to higher combustion temperatures, as observed in Fig. 7. These results denote the carbonization of coke II structure with time on stream, by means of dehydrogenation of aliphatics, deoxygenation and aromatization [35], as well as by its gradually further deposition from the metallic sites, as observed in Fig. 5b–e.

### 3.5. Evolution of coke composition

Raman spectra of deactivated catalysts were performed at different values of time on stream (50, 75, 90 and 100 min) and are shown in Fig. 9. The spectra were deconvoluted into four Lorentzian peaks (G, D1, D3 and D4), ascribed to: (i) G band ( $1575\text{--}1600 \text{ cm}^{-1}$ ), characteristic of graphitic layers [60–62], that is to say, stretching vibrations of  $sp^2$  bonds in aromatic clusters [60,63,64]; (ii) D1 band ( $1350\text{--}1380 \text{ cm}^{-1}$ ), corresponding to the  $sp^2$  bond vibrations close to the edges in the graphitic layers [62,65]; (iii) D3 band ( $1450\text{--}1510 \text{ cm}^{-1}$ ) assigned to amorphous coke in turbostratic fashion due to bond vibrations close to the edges in highly disordered graphitic layers [62,65]; (iv) D4 band ( $\sim 1200 \text{ cm}^{-1}$ ), assigned to  $sp^2\text{--}sp^3$  bond vibrations in disordered graphitic layers, with aliphatic chains [60,62,65,66].

Fig. 10 shows the evolution with time on stream of four characteristic parameters determined from the deconvolution of Raman spectra: (i) G band position ( $\sigma_G$ ,  $\text{cm}^{-1}$ ); (ii) G band FWHM ( $\Gamma_G$ ,  $\text{cm}^{-1}$ ); (iii) ratio of intensities of D1 and G bands ( $I_{D1}/I_G$ ); (iv) size of carbonaceous particle or domain ( $L_a$ , nm). Together analyzed, these four parameters enable the study of the degree of order, aromatization or approximate size of carbonaceous domains [61,67,68]. The determination of the estimated size of carbonaceous particle ( $L_a$ ) was carried out attending to the values of  $\sigma_G$ ,  $\Gamma_G$  and  $I_{D1}/I_G$  [61]. Based on this criterion, the expression in Eq. (10) was used, valid for values of  $L_a < 2 \text{ nm}$ , where coke is more amorphous rather than crystalline [61].

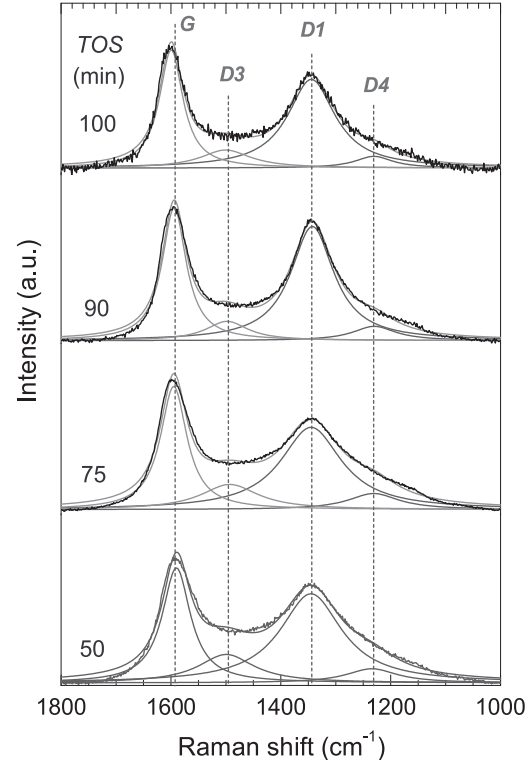


Fig. 9. Evolution with time on stream of the Raman spectra ( $1000\text{--}1800 \text{ cm}^{-1}$ ) of the coke deposited on the catalyst.

$$\frac{I_{D1}}{I_G} = E(\lambda) L_a^2 \quad (10)$$

where  $E(\lambda)$  is a constant dependent on the excitation wavenumber ( $\lambda$ ) employed for the analysis, using  $E(\lambda = 514 \text{ nm}) \approx 0.55$  in this work.

The results of Fig. 10 show the following overall evolution trend with time on stream: increase in the G band position ( $\sigma_G$ ), decrease in the G band width ( $\Gamma_G$ ), increase in the  $I_{D1}/I_G$  area ratio and increase of the carbonaceous domain size ( $L_a$ ). According to the studies in the literature [61,67,69], these results correspond to the carbonization of turbostratic and highly disordered coke (with aliphatic  $sp^3$  bonds), into a more condensed and stacked structure (approaching to the so-called nano-crystalline carbon). During this evolution, the stacking defects of the graphitic layers/clusters decrease at the same rate as these layers/clusters grow and the aliphatic bonds decrease. These results indicate that the deposition of coke on the catalyst (Fig. 8), coexist with that of evolution of its composition (carbonization) towards more ordered (Fig. 10a–c) and bigger (Figs. 5 and 10d) carbonaceous structures.

The most representative FTIR bands were assigned to the following functional groups in the deposited coke [37,63,70–74]: C–O bonds in acetate groups, phenolic esters and/or ethers of type  $\text{C}=\text{C}-\text{O}-\text{C}_{\text{aliphatic}}$  and/or  $\text{C}_{\text{aromatic}}-\text{O}-\text{C}_{\text{aliphatic}}$ ,  $1240\text{--}1260 \text{ cm}^{-1}$ ; symmetric stretching vibrations of  $-\text{CH}_3$  groups in aliphatics,  $1390 \text{ cm}^{-1}$ ; symmetric stretching vibrations of  $\text{O}=\text{C}-\text{O}$  bonds in acetate groups,  $1420\text{--}1430 \text{ cm}^{-1}$ ; bending vibrations in  $-\text{CH}_2$  and  $-\text{CH}_3$  aliphatic

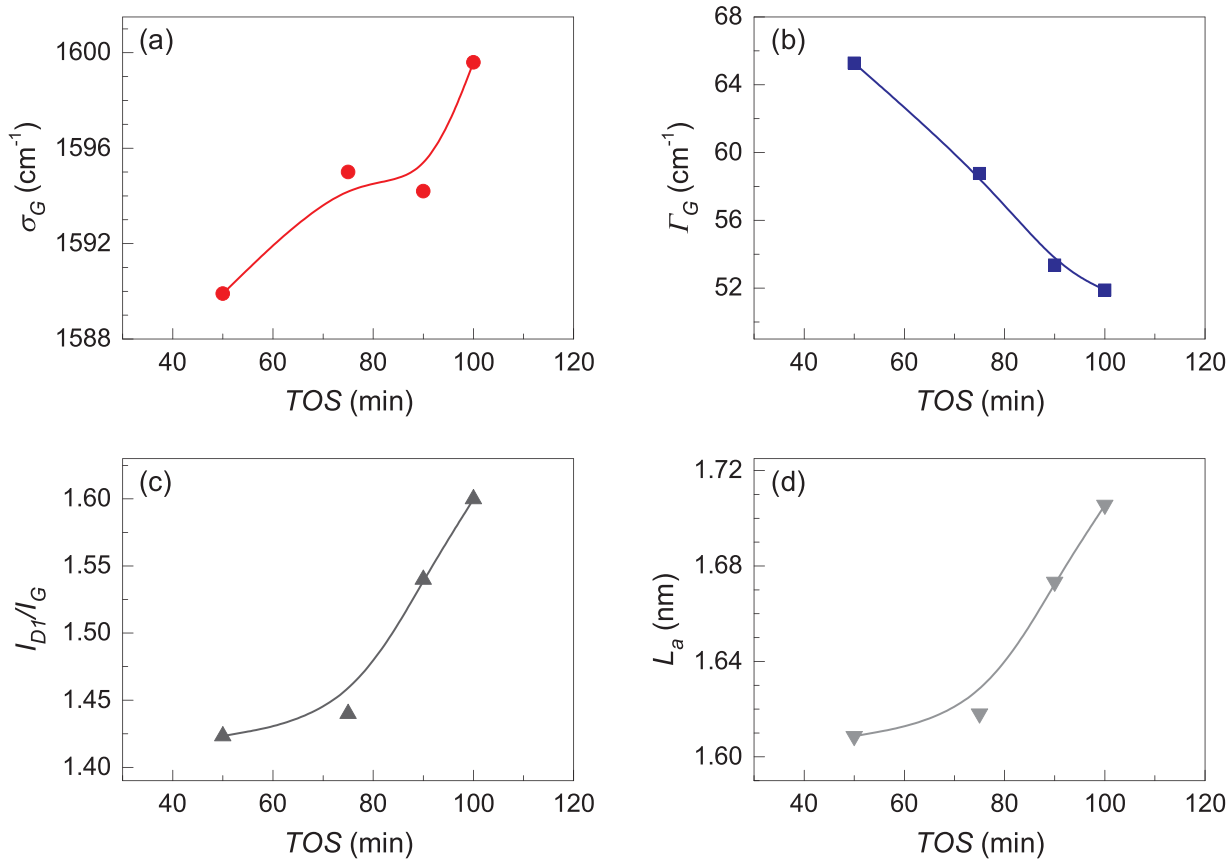


**Fig. 10.** Evolution with time on stream of representative Raman parameters of the coke deposited: G band position ( $\sigma_G$ ) (a); G band width ( $\Gamma_G$ ) (b);  $I_D/I_G$  ratio (c); size of carbon domain ( $L_a$ ) (d).

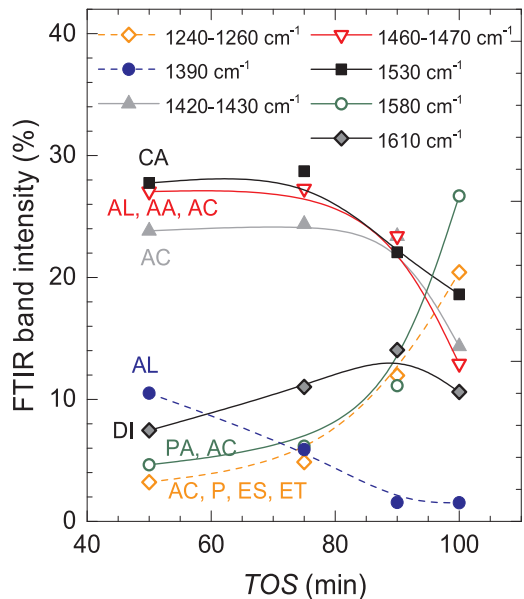


**Fig. 11.** Evolution with time on stream of the relative intensities of several representative FTIR bands corresponding to functional groups in the deposited coke. Abbreviations: alkyl aromatics (AA), aliphatics (AL), acetates (AC), carbonates (CA), dienes (DI), esters (ES), ethers (ET), phenols (P), polyaromatics (PA).

groups, alkyl aromatics and/or symmetric bending vibrations of  $\text{O}=\text{C}-\text{O}$  in acetate groups,  $1460-1470 \text{ cm}^{-1}$ ; asymmetric stretching vibrations of  $\text{O}=\text{C}-\text{O}$  in groups such as carbonates,  $1530 \text{ cm}^{-1}$ ; polycondensed aromatics ('coke band') and/or asymmetric stretching

vibrations of  $\text{O}=\text{C}-\text{O}$  bonds in acetate groups,  $1580 \text{ cm}^{-1}$ ; dienes and/or conjugated double bonds,  $1610 \text{ cm}^{-1}$ ; C–H in  $-\text{CH}_2$  aliphatic groups,  $2855 \text{ cm}^{-1}$ ; C–H in  $-\text{CH}_3$  aliphatic groups,  $2870 \text{ cm}^{-1}$ ; C–H in  $-\text{CH}$  and  $-\text{CH}_2$  aliphatic groups,  $2920 \text{ cm}^{-1}$ ; C–H in  $-\text{CH}_3$  aliphatic groups,  $2960 \text{ cm}^{-1}$ . This assignment reveals a high heterogeneity of functional groups in coke and thus difficulty to univocally assign FTIR bands to particular species. The FTIR spectra, shown in Fig. SI-1 as Supporting Information, were deconvoluted into Lorentzian peaks in the mentioned band positions, and the relative area percentage of each peak was calculated with respect to the whole area below the  $1100-3200 \text{ cm}^{-1}$  region [37,43]. Fig. 11 shows the evolution with time on stream of these relative intensities of the most representative bands. The results confirm the previous discussed carbonization process of the coke, as the content of aliphatics (AL) ( $1390 \text{ cm}^{-1}$ ) is continuously decreased with time on stream, which are transformed into dienes (DI) ( $1610 \text{ cm}^{-1}$ ) and the latter are subsequently transformed into polycondensed aromatic structures (PA) ( $1580 \text{ cm}^{-1}$ ), whose content is significantly increased with time on stream. This reaction in series towards coke carbonization is suggested as well by the maximum observed in the content of dienes (DI) ( $1610 \text{ cm}^{-1}$ ). At short values of time on stream, coke has a more oxygenated nature, with a higher content in acetates (AC) ( $1420-1430 \text{ cm}^{-1}$ ) and carbonates (CA) ( $1530 \text{ cm}^{-1}$ ), whose content is decreased with time on stream during the coke carbonization process. Owing to the assignment of several functional groups in the same position in some bands, the content of oxygenates in the band at  $1240-1260 \text{ cm}^{-1}$ , namely esters (ES) and/or ethers (ET), is expected to decrease with time on stream, in line with the observed evolution for acetates (AC) ( $1420-1430 \text{ cm}^{-1}$ ) and carbonates (CA) ( $1530 \text{ cm}^{-1}$ ). Moreover, owing to this overlapping in several group assignments, the contribution to the FTIR intensity of alkyl aromatics (AA) in the band at  $1460-1470 \text{ cm}^{-1}$ , and phenols (P)

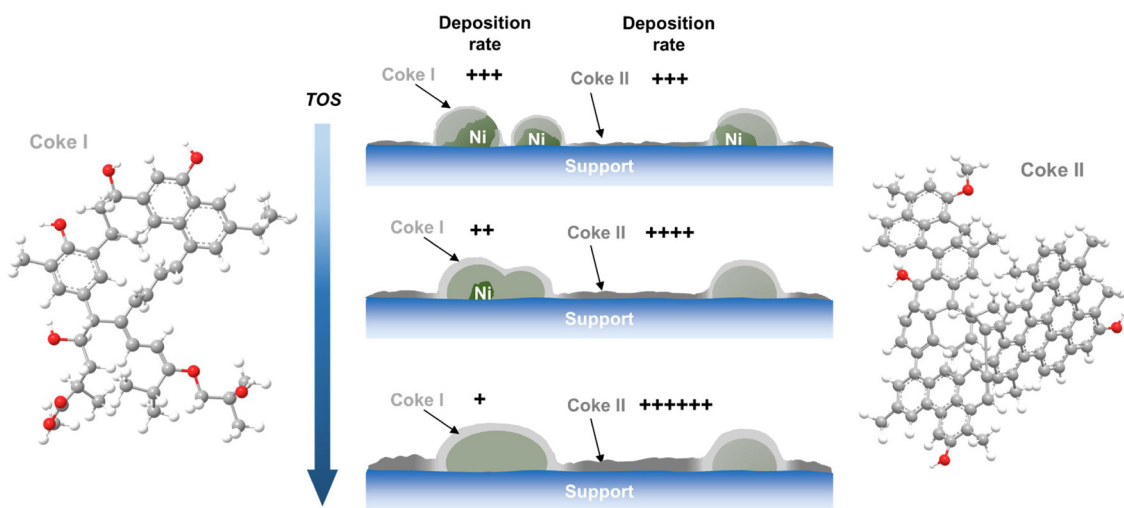


Fig. 12. Proposed molecular structures, location and deposition rate of coke with time on stream, based on its characterization.

in the band at 1240–1260  $\text{cm}^{-1}$  is not clear. Nevertheless, their content is expected to decrease with time on stream, owing to (i) the alkylated nature of alkyl aromatics and the fact that aliphatics content is decreased in Fig. 11, and (ii) the oxygenated nature of phenols and the fact that oxygenates content is overall decreased in Fig. 11, thus contributing to the coke dehydrogenation and deoxygenation along with the carbonization process.

#### 4. Discussion

The use of several characterization techniques at different values of time on stream during the steam reforming of volatiles from biomass pyrolysis enables the identification of two phenomena which contribute to catalyst deactivation: (i) Ni sintering, and to a greater extent, (ii) coke deposition, whose content, chemical nature and location change with time on stream. The catalyst performance in terms of reaction indices has shown two differentiated stages of deactivation: (i) a mild and steady deactivation up to ca. 50 min on stream, followed by (ii) an exponential deactivation from ca. 50 min on stream. Based on these results, Fig. 12 shows a general scheme of the catalyst deactivation, in terms of Ni sintering and coke deposition.

The temperature used in this work (600 °C) is similar to the Tamman temperature of pure Ni (590 °C); however, the presence of steam in the reaction medium and the submission of the catalyst in these operating conditions during 100 min on stream unavoidably leads to its sintering. First, sintering takes place rapidly from the fresh reduced catalyst at the beginning of the reaction. Subsequently, during the reaction Ni particles sinter at an approximately linear rate of ca. 5–8  $\text{nm h}^{-1}$ , as observed from XRD (Fig. 3) and TEM results (Table 4). On the other hand, content of the coke deposited has shown to increase with time on stream (Fig. 8), with an increase in the size of carbonaceous structures (Fig. 10d). This deposition takes place both on the Ni particles (coke I) and on the support (coke II), as depicted in Fig. 12. However, their formation rate is changed with time on stream. At low values of time on stream, coke starts both covering the Ni particles and the support at a similar formation rate, according to the results of TEM (Fig. 5b) and TPO (Fig. 8). From 50 min on stream, as the coverage of the Ni particles is increased, the formation rate of coke I is decreased. This increase in the coverage of Ni sites and partial blocking of micropores hinders the access of reactants to them, and leads to a more rapid catalyst deactivation (Fig. 1), as the conversion of biomass pyrolysis volatiles and yields of  $\text{H}_2$  and  $\text{CO}_2$  decrease more rapidly, whereas these of  $\text{CH}_4$  and  $\text{C}_2\text{--C}_4$  increase quicker. Meanwhile, as the deposition of coke I is decreased, coke deposition is favored further from Ni particles (coke II), whose formation rate is higher than that at low values of time on

stream, according to the results of TEM (Fig. 5c–e) and TPO (Fig. 8). The simultaneous formation of coke I and II and their changes in the formation rate with time on stream are responsible of the increasing and decreasing trends of the surface area and porosity with time on stream (Table 3).

The differences in location between coke I and II also influence on their composition, according to the results of TPO (Table 5), Raman spectroscopy (Fig. 10) and FTIR spectroscopy (Fig. 11). Thus, as depicted in Fig. 12, coke I has a lighter nature, with a higher oxygenated nature (O/C ratio) and hydrogenated nature (H/C ratio or proportion of aliphatics with respect to aromatics), due to its proximity of coke to metallic sites, which catalyze coke combustion and/or gasification and thus impedes further coke carbonization. On the other hand, coke II has a higher content of structured aromatics and lower of hydrogen and oxygen (Fig. 12), as it is spatially further from the metal particles, thus its combustion/gasification not being catalyzed and leading to a more carbonized structure compared to that of coke I. The content of coke II (Fig. 8), as well as the proportion of phenols within the overall coke structure (Fig. 11), increase considerably with time on stream, thus concluding that coke II possesses more phenols in its structure than coke I. In line with previous works [37,75,76], an increase in the proportion of phenols in the reaction medium and coke structure leads to an increase in coke formation and catalyst deactivation, as corroborated in Fig. 1. Moreover, the formation of coke II coexists with its carbonization with time on stream, as proved by the results of Table 5.

The aforementioned results of the catalyst deactivation in the in-line steam reforming of biomass pyrolysis oxygenated volatiles can be correlated with the results in the literature about deactivation of other Ni-based catalysts in the steam reforming of bio-oil. In the steam reforming of bio-oil, the main precursors of the coke encapsulating the Ni sites (coke I) are considered to be the phenols (including methoxyphenols) which, after being adsorbed on the metal sites, undergo condensation mechanisms towards amorphous and encapsulating coke structures [16]. Considering that both the deactivation rate (Fig. 1) and rate of formation of the coke deposited on the support (coke II) (Fig. 8) are increased more rapidly in a similar trend from 50 min on stream, coke II is thought to be formed from thermal decomposition of oxygenated volatiles, which is promoted as the catalyst deactivates and the reforming reactions are disfavored. These thermal decomposition reactions also explain the increase in the yield of light hydrocarbons, i.e.  $\text{CH}_4$  and  $\text{C}_2\text{--C}_4$  hydrocarbons.

#### 5. Conclusions

The steam reforming of biomass pyrolysis volatiles in this work

shows two main causes of catalyst deactivation, in the form of sintering of Ni and, more significantly, coke deposition. The operating conditions used in this work were satisfactory to attain conversions above 98% and H<sub>2</sub> yields above 90% within the first 50 min on stream, but at the same time led to the continuous sintering of the Ni on the catalyst. The rate of sintering was approximately of 5–8 nm h<sup>−1</sup>, as proved by XRD and TEM techniques. The formation and growth of the coke deposited on the catalyst were studied by means of the combination of multiple techniques, resulting in two deactivation stages: (i) < 50 min, coke starts both covering the Ni particles (encapsulating coke or I) and the support (coke II) at similar formation rates, whose influence in deactivation is still not very noticeable; and (ii) > 50 min, the rate of formation of encapsulating coke decreases, which leads to a significant decrease in the catalyst activity, and thus coke is preferentially deposited on the support and the vicinities of the Ni particles (coke II), whose formation rate is significantly increased. The main precursors of the coke covering the Ni sites (coke I) are the biomass pyrolysis oxygenates which, after being adsorbed on the metal sites, undergo further condensation mechanisms towards amorphous and encapsulating coke. Considering the proximity of this coke to Ni, which catalyze coke combustion and/or gasification, the further carbonization of this coke is hindered and thus presents a similar chemical nature with time on stream, with a higher hydrogenated and oxygenated nature. On the other hand, the coke deposited in the support (II) is formed from the thermal decomposition of oxygenated volatiles, whose route is promoted as the catalyst deactivates and the reforming reactions are disfavored. Considering its further location from Ni sites, it possesses a more structured aromatic and less oxygenated nature, and is progressively carbonized with time on stream.

These results open an interesting work field into the process, aiming the minimization of the Ni sintering and the deposition of encapsulating coke. Both objectives can be achieved decreasing the temperature and tuning other operating conditions, but may disfavor the steam reforming route and lower the H<sub>2</sub> production. Considering the relevance of the feed composition on coke formation, some other interesting proposals are tuning the operating conditions of the pyrolysis process prior to the steam reforming step, or co-feeding of biomass with wastes such as polyolefins into the in-line pyrolysis-reforming system.

## Acknowledgments

This work was carried out with the support of the Ministry of Economy and Competitiveness of the Spanish Government, some co-founded with ERDF funds (CTQ2013-46172-P, CTQ-2015-69436-R (MINECO/FEDER, UE), and CTQ2016-79646-P) and the Basque Government (IT748-13). A. Ochoa is grateful for his predoctoral grant from the Department of Education, Language Policy and Culture of the Basque Government (PRE\_2016\_2\_0129). A. Arregi thanks the University of the Basque Country for his postgraduate grant (UPV/EHU 2017). The technical and human support provided by SGIker (UPV/EHU, MICINN, GV/EJ, ERDF and ESF) is greatly acknowledged.

## Appendix A. Supplementary data

Supplementary material related to this article can be found, in the online version, at doi:<https://doi.org/10.1016/j.apcatb.2018.04.002>.

## References

- [1] W. Nabgan, T.A. Tuan Abdullah, R. Mat, B. Nabgan, Y. Gambo, S. Triwahyono, Int. J. Hydrogen Energy 41 (2016) 22922–22931.
- [2] W. Nabgan, T.A. Tuan Abdullah, R. Mat, B. Nabgan, Y. Gambo, M. Ibrahim, A. Ahmad, A.A. Jalil, S. Triwahyono, I. Saeh, Renew. Sustain. Energy Rev. 79 (2017) 347–357.
- [3] S. Ayalur Chattanathan, S. Adhikari, N. Abdoulmoumine, Renew. Sustain. Energy Rev. 16 (2012) 2366–2372.
- [4] I. Dincer, Int. J. Hydrogen Energy 37 (2012) 1954–1971.
- [5] R. Parajuli, T. Dalgaard, U. Jørgensen, A.P.S. Adamsen, M.T. Knudsen, M. Birkved, M. Gylling, J.K. Schjørring, Renew. Sustain. Energy Rev. 43 (2015) 244–263.
- [6] T. Berdugo Vilches, J. Marinkovic, M. Seemann, H. Thunman, Energy Fuels 30 (2016) 4848–4857.
- [7] K. Umeki, K. Yamamoto, T. Namioka, K. Yoshikawa, Appl. Energy 87 (2010) 791–798.
- [8] E. Madadian, V. Orsat, M. Lefsrud, Energy Fuels 31 (2017) 4045–4053.
- [9] F.L. Chan, A. Tanksale, Appl. Catal. B 187 (2016) 310–327.
- [10] S. Rapagnà, K. Gallucci, M. Di Marcello, P.U. Foscolo, M. Nacken, S. Heidenreich, M. Matt, Fuel 97 (2012) 718–724.
- [11] P. Iovane, A. Donatelli, A. Molino, Biomass Bioenergy 56 (2013) 423–431.
- [12] A. Erkiaga, G. Lopez, M. Amutio, J. Bilbao, M. Olazar, Chem. Eng. J. 237 (2014) 259–267.
- [13] P. Fu, W. Yi, Z. Li, X. Bai, A. Zhang, Y. Li, Z. Li, Int. J. Hydrogen Energy 39 (2014) 13962–13971.
- [14] A. Remiro, A. Arandia, J. Bilbao, A.G. Gayubo, Energy Fuels 31 (2017) 7147–7156.
- [15] F. Bimbela, J. Ábreo, R. Puerta, L. García, J. Arauzo, Appl. Catal. B 209 (2017) 346–357.
- [16] B. Valle, B. Aramburu, M. Olazar, J. Bilbao, A.G. Gayubo, Fuel 216 (2018) 463–474.
- [17] X. Xiao, J. Cao, X. Meng, D.D. Le, L. Li, Y. Ogawa, K. Sato, T. Takarada, Fuel 103 (2013) 135–140.
- [18] F. Chen, C. Wu, L. Dong, A. Vassallo, P.T. Williams, J. Huang, Appl. Catal. B 183 (2016) 168–175.
- [19] J. Zou, H. Yang, Z. Zeng, C. Wu, P.T. Williams, H. Chen, Int. J. Hydrogen Energy 41 (2016) 10598–10607.
- [20] L. Dong, C. Wu, H. Ling, J. Shi, P.T. Williams, J. Huang, Fuel 188 (2017) 610–620.
- [21] X.-Y. Zhao, J. Ren, J.-P. Cao, F. Wei, C. Zhu, X. Fan, Y.-P. Zhao, X.-Y. Wei, Energy Fuels 31 (2017) 4054–4060.
- [22] A. Erkiaga, G. Lopez, I. Barberias, M. Artetxe, M. Amutio, J. Bilbao, M. Olazar, J. Anal. Appl. Pyrolysis 116 (2015) 34–41.
- [23] I. Barberias, G. Lopez, J. Alvarez, M. Artetxe, A. Arregi, J. Bilbao, M. Olazar, Chem. Eng. J. 296 (2016) 191–198.
- [24] I. Barberias, G. Lopez, M. Artetxe, A. Arregi, L. Santamaría, J. Bilbao, M. Olazar, J. Anal. Appl. Pyrolysis 122 (2016) 502–510.
- [25] A. Arregi, G. Lopez, M. Amutio, I. Barberias, J. Bilbao, M. Olazar, RSC Adv. 6 (2016) 25975–25985.
- [26] I. Barberias, G. Lopez, M. Artetxe, A. Arregi, J. Bilbao, M. Olazar, Energy Convers. Manage. 156 (2018) 575–584.
- [27] A. Arregi, M. Amutio, G. Lopez, M. Artetxe, J. Alvarez, J. Bilbao, M. Olazar, Energy Convers. Manage. 136 (2017) 192–201.
- [28] R. Trane, S. Dahl, M.S. Skjøth-Rasmussen, A.D. Jensen, Int. J. Hydrogen Energy 37 (2012) 6447–6472.
- [29] B. Valle, B. Aramburu, A. Remiro, J. Bilbao, A.G. Gayubo, Appl. Catal. B 147 (2014) 402–410.
- [30] F.G.E. Nogueira, P.G.M. Assaf, H.W.P. Carvalho, E.M. Assaf, Appl. Catal. B 160–161 (2014) 188–199.
- [31] J.J. Spivey, Fuel Cells: Technologies for Fuel Processing, Elsevier, Amsterdam, 2011, pp. 285–315.
- [32] M.D. Argyle, C.H. Bartholomew, Catal. Today 5 (2015) 145–269.
- [33] A. Arregi, G. Lopez, M. Amutio, M. Artetxe, I. Barberias, J. Bilbao, M. Olazar, Fuel 216 (2018) 233–244.
- [34] J. Vicente, J. Ereña, C. Montero, M.J. Azkotai, J. Bilbao, A.G. Gayubo, Int. J. Hydrogen Energy 39 (2014) 18820–18834.
- [35] J. Vicente, C. Montero, J. Ereña, M.J. Azkotai, J. Bilbao, A.G. Gayubo, Int. J. Hydrogen Energy 39 (2014) 12586–12596.
- [36] C. Montero, A. Ochoa, P. Castaño, J. Bilbao, A.G. Gayubo, J. Catal. 331 (2015) 181–192.
- [37] A. Ochoa, B. Aramburu, B. Valle, D. Resasco, J. Bilbao, A.G. Gayubo, P. Castaño, Green Chem. 19 (2017) 4315–4333.
- [38] P. Djinović, I.G. Osojnik Črnivec, B. Erjavec, A. Pintar, Appl. Catal. B 125 (2012) 259–270.
- [39] J.A. Medrano, M. Oliva, J. Ruiz, L. García, J. Arauzo, Energy 36 (2011) 2215–2224.
- [40] A. Remiro, B. Valle, B. Aramburu, A.T. Aguayo, J. Bilbao, A.G. Gayubo, Ind. Eng. Chem. Res. 52 (2013) 17087–17098.
- [41] A. Remiro, B. Valle, A.T. Aguayo, J. Bilbao, A.G. Gayubo, Fuel Process. Technol. 115 (2013) 222–232.
- [42] J. Góralski, J. Grams, T. Paryjczak, I. Rzeźnicka, Carbohydr. Res. 40 (2002) 2025–2028.
- [43] A. Ochoa, I. Barberias, M. Artetxe, A.G. Gayubo, M. Olazar, J. Bilbao, P. Castaño, Appl. Catal. B 209 (2017) 554–565.
- [44] M. Amutio, G. Lopez, M. Artetxe, G. Elordi, M. Olazar, J. Bilbao, Resour. Conserv. Recycl. 59 (2012) 23–31.
- [45] K.M. Hardiman, C.G. Cooper, A.A. Adesina, R. Lange, Chem. Eng. Sci. 61 (2006) 2565–2573.
- [46] C.V. Satyanarayana, D. Srikant, H.R. Gurav, V.V. Ranade (Ed.), Industrial Catalytic Processes for Fine and Specialty Chemicals, Elsevier, Amsterdam, 2016, pp. 187–219.
- [47] J.R. Rostrup-Nielsen, K. Pedersen, J. Sehested, Appl. Catal. A 330 (2007) 134–138.
- [48] J. Sehested, A. Carlsson, T.V.W. Janssens, P.L. Hansen, A.K. Datye, J. Catal. 197 (2001) 200–209.
- [49] S. Wang, G.Q. Lu, Ind. Eng. Chem. Res. 38 (1999) 2615–2625.
- [50] A.G. Gayubo, J. Vicente, J. Ereña, L. Oar-Arteta, M.J. Azkotai, M. Olazar, J. Bilbao, Appl. Catal. A 483 (2014) 76–84.
- [51] B. Valle, A. Remiro, A.T. Aguayo, J. Bilbao, A.G. Gayubo, Int. J. Hydrogen Energy 38 (2013) 1307–1318.
- [52] V. Shanmugam, R. Zapf, S. Neuberg, V. Hessel, G. Kolb, Appl. Catal. B 203 (2017)

859–869.

[53] N. Latorre, F. Cazaña, V. Martínez-Hansen, C. Royo, E. Romeo, A. Monzón, *Catal. Today* 172 (2011) 143–151.

[54] D.L. Trimm, *Catal. Today* 49 (1999) 3–10.

[55] S. Helveg, J. Sehested, J.R. Rostrup-Nielsen, *Catal. Today* 178 (2011) 42–46.

[56] A.M. Karim, Y. Su, J. Sun, C. Yang, J.J. Strohm, D.L. King, Y. Wang, *Appl. Catal. B* 96 (2010) 441–448.

[57] R. Trane-Restrup, D.E. Resasco, A.D. Jensen, *Catal. Sci. Technol.* 3 (2013) 3292–3302.

[58] F. Wang, Y. Li, W. Cai, E. Zhan, X. Mu, W. Shen, *Catal. Today* 146 (2009) 31–36.

[59] A. Ochoa, Á. Ibarra, J. Bilbao, J.M. Arandes, P. Castaño, *Chem. Eng. Sci.* 171 (2017) 459–470.

[60] J. Schwan, S. Ulrich, V. Batori, H. Ehrhardt, S.R.P. Silva, *J. Appl. Phys.* 80 (1996) 440–447.

[61] J. Robertson, *Mater. Sci. Eng. R* 37 (2002) 129–281.

[62] A. Sadezky, H. Muckenhuber, H. Grothe, R. Niessner, U. Pöschl, *Carbohydr. Res.* 43 (2005) 1731–1742.

[63] P. Castaño, G. Elordi, M. Olazar, A.T. Aguayo, B. Pawelec, J. Bilbao, *Appl. Catal. B* 104 (2011) 91–100.

[64] B. Valle, P. Castaño, M. Olazar, J. Bilbao, A.G. Gayubo, *J. Catal.* 285 (2012) 304–314.

[65] J. Source, A. Quinsac, Y. Leconte, O. Sublemontier, W. Porcher, C. Haon, A. Bordes, E. De Vito, A. Boulineau, S. Jouanneau Si Larbi, N. Herlin-Boime, C. Reynaud, *ACS Appl. Mater. Interfaces* 7 (2015) 6637–6644.

[66] P. Minutolo, M. Commodo, A. Santamaría, G. De Falco, A. D'Anna, *Carbohydr. Res.* 68 (2014) 138–148.

[67] A.C. Ferrari, D.M. Basko, *Nat. Nanotechnol.* 8 (2013) 235–246.

[68] C. Pardanaud, C. Martin, G. Giacometti, N. Mellet, B. Pégourié, P. Roubin, *Thin Solid Films* 581 (2015) 92–98.

[69] A.C. Ferrari, *Solid State Commun.* 143 (2007) 47–57.

[70] B. Stuart, *Infrared Spectroscopy: Fundamentals and Applications*, John Wiley & Sons, New York, 2004.

[71] E. Pretsch, P. Bühlmann, M. Badertscher, *Structure Determination of Organic Compounds: Tables of Spectral Data*, 4th ed., Springer, Berlin, 2009.

[72] L.V. Mattos, G. Jacobs, B.H. Davis, F.B. Noronha, *Chem. Rev.* 112 (2012) 4094–4123.

[73] W. Xu, Z. Liu, A.C. Johnston-Peck, S.D. Senanayake, G. Zhou, D. Stacchiola, E.A. Stach, J.A. Rodriguez, *ACS Catal.* 3 (2013) 975–984.

[74] A. Ochoa, B. Aramburu, M. Ibáñez, B. Valle, J. Bilbao, A.G. Gayubo, P. Castaño, *ChemSusChem* 7 (2014) 2597–2608.

[75] A.G. Gayubo, B. Valle, A.T. Aguayo, M. Olazar, J. Bilbao, *J. Chem. Technol. Biotechnol.* 85 (2010) 132–144.

[76] P.J. Ortiz-Toral, J. Satrio, R.C. Brown, B.H. Shanks, *Energy Fuels* 25 (2011) 3289–3297.